Complexation strength between organic carbon and transition metal ions dominates the photochemical conversion of SO_2 to sulfates

Shaojie Yang, Shiwei Lai, Jianwei Zheng, Hao Na, Fu Li, Wangjin Yang, Chong Han

School of Metallurgy, Northeastern University, Shenyang, 110819, China

Correspondence: Chong Han (hanch@smm.neu.edu.cn)

Abstract

The photooxidation of SO_2 on organic carbon (OC) is a critical pathway for sulfate formation, yet the role of interactions between OC and transition metal ions (TMIs) in this process remains scarcely understood. We systematically investigated potential influences of TMIs (Fe^{3+}, Cu^{2+} and Mn^{2+}) on the conversion of SO_2 to sulfates on OC from coal combustion under irradiation. For OC and its coexistence with TMIs under experimental conditions adopted here, the steady-state uptake coefficients of SO_2 and sulfate masses were $(0.39-22.24) \times 10^{-6}$ and $(2.36-26.05) \times 10^{-3}$ mg, respectively. Fe^{3+} exhibited a significantly antagonistic effect, whereas Cu^{2+} and Mn^{2+} enhanced SO_2 uptake and sulfate generation on OC. Spectroscopic evidences, including absorbance decreasing and fluorescence quenching, confirmed the complexes formation of TMI with chromophores in OC. Fe^{3+} owned the strongest binding affinity with chromophores, followed by Cu^{2+} and Mn^{2+}. This variation in the coordination strength dominated the generation of reactive species, such as free electrons (e^-), superoxide radicals ($\bullet O_2^-$), H_2O_2 and hydroxyl radicals (•OH), and •OH acted as a pivotal trigger to drive the sulfate production. Extended investigations confirmed a good linear relationship between •OH intensity (I) and sulfate mass ($M_{sulfates}$): $M_{sulfates} = (1.68 \pm 0.11) \times 10^{-2} \times I - (0.43 \pm 0.08) \times 10^{-2}$, demonstrating that the regulatory effects of metal ions on the sulfate production were generally governed through their ability to suppress or facilitate the •OH generation.

Graphical abstract:

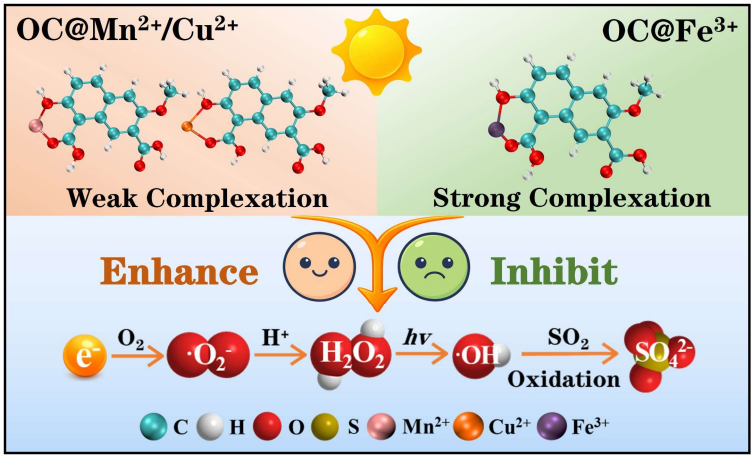

1 Introduction

Fine particulate matter ($PM_{2.5}$) is a complex mixture of inorganic and organic species, and plays a central role in the persistent haze events (Fan et al., 2016; Huang et al., 2014; Peng et al., 2021). The rapid accumulation of sulfates in $PM_{2.5}$ significantly influences atmospheric radiative forcing, air quality and human health (Zhang et al., 2020a; Salana et al., 2024). Sulfates primarily stem from SO_2 oxidation, including reactions with hydroxyl radicals (•OH) in the gas phase and aqueous oxidation in cloud and fog droplets involving various oxidizing species (Tsona and Du, 2019; Liu et al., 2020a; Jiang et al., 2009; Hoyle et al., 2016; Liu and Abbatt, 2021). However, only considering these pathways usually leads to a pronounced gap between the modeled and observed sulfate concentrations during the haze events (Li et al., 2017; Eckhardt et al., 2015; Zheng et al., 2015).

To bridge this gap, several heterogeneous pathways have been proposed, involving reactions of SO_2 on $PM_{2.5}$, mineral dust (e.g., Arizona test dust and metal oxides), inorganic salt (e.g., nitrates and NaCl), soot and organic aerosols (Zhang et al., 2020c; Zhang et al., 2019; Dupart et al., 2012; Yang et al., 2024a; Cao et al., 2024b; Zhang et al., 2022). Although these heterogeneous reactions have narrowed the discrepancies between model prediction and field observation concentrations of sulfates, substantial uncertainties and controversies still remain (Wang et al., 2014). This may be attributed to the fact that most studies mainly focus on simplified single-component systems and overlook the extreme complexity of multicomponent aerosols under realistic atmospheric conditions. Recent evidence highlighted that the potential

interactions among distinct components in aerosols can significantly influence the transformation pathways of atmospheric pollutants (Zhang and Chan, 2023; Zhang et al., 2023). For instance, organic carbon (OC) in soot can donate electrons to elemental carbon (EC) and enhance the electron-hole separation under irradiation, thereby generating more •OH and promoting the conversion of SO_2 to sulfates (Zhu et al., 2022). OC-derived photosensitizers activated both O_2 and Cl^- in NaCl-OC under ultraviolet light, producing •OH and Cl• that synergistically oxidized SO_2 to sulfates (Tang et al., 2023).

OC from coal combustion can serve as a photosensitive electron donor under irradiation, initiating the formation of reactive oxygen species (ROS), which subsequently oxidized SO_2 to sulfates (Yang et al., 2025). In atmospheric aerosols, OC often coexisted with various TMIs, especially in some regions influenced by the combustion, vehicular emissions, and industrial processes (Yang et al., 2024b; Deng et al., 2022; Zhang et al., 2020b; Shiraiwa et al., 2017; Hua et al., 2025). This coexistence was not a simple superposition of their specific roles. OC usually contained diverse functional groups such as carboxyl, hydroxyl and carbonyl moieties, which can interact with TMIs via the complexation, metal-proton ion exchange and electrostatic adsorption, forming organometallic complexes in aerosols (Li et al., 2022; Wang et al., 2021c; Wang et al., 2021b). Furthermore, the binding strength between OC and TMIs varied with the specific type of TMIs, which was related to the differences in ionic radius, oxidation state and electronic configuration that influenced coordination chemistry and redox reactivity (Wang et al., 2021a; Pan et al., 2020). Fe, Cu and Mn are the most abundant transition metals in atmospheric aerosols and cloud water (Singh and Gupta, 2017). Their soluble ionic forms, including Fe^{3+}, Cu^{2+} and Mn^{2+}, can catalyze or regulate SO_2 oxidation and sulfate formation (Liu et al., 2025). The potential roles of OC and these TMIs in the heterogeneous photochemical oxidation of SO_2 haven't been systematically investigated, which may restrict the exact incorporation of OC photochemistry into the sulfate formation prediction models.

Our previous work mainly focused on the intrinsic photo-reactivity of OC and its dependence on the physicochemical properties (Yang et al., 2025). In this study, laboratory experiments and theoretical calculations were conducted to elucidate the influences of TMIs (Fe^{3+}, Mn^{2+} and Cu^{2+}) on the photooxidation of SO_2 to sulfates on OC from coal combustion. Differences in the photochemical activity were quantified by measuring SO_2 uptake coefficients and sulfate yields.

Changes in the optical properties were examined to evaluate the potential interactions between OC and TMIs. Mechanism insights into the reactive species generation, including e^-, $\bullet O_2^-$, H_2O_2 and •OH, clarified how these interactions regulated the SO_2 photooxidation. Finally, further investigation involving multiple metal ions commonly within atmospheric aerosols highlighted the broader significance of OC and TMIs interactions in the sulfate formation.

2 Materials and methods

2.1 Preparation of OC and OC@TMIs samples

As shown in Fig. S1, OC was obtained with a custom combustion and sampling apparatus. The coal in the combustion experiment originated from Shanxi Province, China. The details of OC sampling and preparation are provided in Text S1. The background concentrations of Fe, Mn and Cu in OC were measured through ICP-MS, and they varied in the range of 1.23−7.70 μg L^{-1}. The details of ICP-MS measurements are provided in Text S2. 1 mL of the extracted OC solution was dropped onto 6.0 × 1.5 cm prebaked quartz-fiber filters, and the solvents were dried under a N_2 stream (100 mL min^{-1}) in the dark at 298 K.

The sources and purities of salt chlorides used here are provided in Text S3. Stock solutions of metal salts (1.5 mM, in ultrapure water) were mixed with the OC solution at a 1:2 volume ratio, yielding mixtures containing 0.5 mM metal ions and 543.9 ± 35.4 μgC mL^{-1} (Fig. S1). This metal-ion concentration was close to the levels reported in heavily polluted atmospheric conditions (Li et al., 2022). Each mixture was ultrasonicated for 30 min at 25 ℃ in the dark. The resulting products were designated as OC@TMIs, including OC@Fe^{3+}, OC@Cu^{2+} and OC@Mn^{2+}. Here, OC@TMIs referred to the actual sample prepared by introducing a specific TMI into OC. OC+TMIs was defined as a reference sample, where the interaction between OC and TMIs was assumed to be nonoccurrence. The property of OC+TMIs represented the arithmetic sum of that measured separately for OC and metal ion. Thus, OC+TMIs was utilized as a reference for evaluating synergistic or antagonistic effects of OC and TMIs. In the OC@NaCl control experiment, the NaCl concentration was 1.5 mM. 1.5 mL of the mixed solution was deposited on the inner surface of a quartz flow tube (20 cm length, 1.0 cm inner diameter). The flow tube was rotated slowly to ensure the uniform wetting of the surface. The coating was obtained by drying the samples under a N_2 stream (100 mL min^{-1}) in the dark

environment at 298 K to prevent photochemical interference. Because a single sample could not be used sequentially for all experimental measurements, separate subsamples from the same initial batch of OC@TMIs were used to minimize potential variability.

2.2 Flow tube experiments and SO_2 uptake coefficients

The SO_2 uptake experiments were performed at ambient pressure in a horizontal cylindrical quartz flow tube reactor (34 cm length, 1.6 cm i.d.), as shown in Fig.S1. The details of the flow reactor and reaction procedure are given in Text S4. The changes in the SO_2 concentration were measured with a SO_2 analyzer (Thermo 43i). The calculation of the SO_2 uptake coefficient is described in Text S5.

2.3 Analysis methods

2.3.1 Measurements of sulfate products

The functional group changes during the photochemical reaction of SO_2 on the samples were characterized using in situ attenuated total reflection infrared (ATR-IR) spectroscopy (Nicolet iS50, Thermo Scientific), which was equipped with a mercury-cadmium-telluride (MCT) detector. Descriptions of experimental process are given in Text S6.

The sulfate ions were quantified using an ion chromatography (IC) system (CIC-D120+, Shenghan) with an analytical column (AS11-HC, Thermo) and a conductivity detector. The testing procedures are described in Text S7.

2.3.2 Optical property measurements

The optical properties of OC, TMIs, and OC@TMIs were analyzed using the UV-vis absorption spectroscopy and the excitation-emission matrix (EEM) fluorescence spectroscopy. The UV-vis spectra were recorded by the UV-vis spectrophotometer (UV-2550, Shimadzu) with a 1.0 cm pathlength cell in the wavelength range of 200−600 nm. A mixed solution of methanol and water (2:1, v/v) was used as the blank background. Samples were diluted to one-fifteenth of the original concentrations. UV-vis analysis was carefully performed under identical testing conditions to minimize handling-related variations.

The EEM fluorescence spectra were measured via a fluorescence spectrophotometer (FP8550, Jasco) at 700 V voltage and 3-D mode in the wavelength ranges of 200−400 nm for excitation (Ex.) and 300−520 nm for emission (Em.). The fluorescence spectra were recorded at 5 nm intervals and a scan speed of 2400 nm min^{-1} in a 1 cm path-length quartz cuvette.

Samples were diluted to one-fifteenth of the original concentrations to minimize the inner-filter effect (IFE) and reabsorption artifacts, which can distort the excitation−emission spectra at high sample concentrations. Instrument calibration, correction for inner-filter effects and normalization of fluorescence intensity to the Raman units (RU) of solvent were conducted before EEM spectral analysis. The EEM data were modeled with the parallel factor analysis (PARAFAC) through the DOMFluo toolbox (version 0.2.0) for MATLAB. Based on the evaluation of 2−4 components using EEM profiles and residual error patterns, a 3-component model was ultimately selected (Fig. S4).

2.3.3 Electrochemical measurements

The electron donating capacities (EDC) of the samples were determined using an electrochemical workstation (CHI760F, Shanghai Chenhua Co., Ltd.) equipped with a three-electrode system. The testing procedures are described in Text S8. The EDC was calculated as the following Eq. (1) (Ma et al., 2024),

$$EDC = \frac{\int \frac{I_{ox}}{F} d_t}{m_{organic\ carbon}} \quad (1)$$

where I_{ox} means the OC oxidation curves; F is the constant of Faraday, which is equal to 96485 s A mol^{-1} e^-; $m_{organic\ carbon}$ represents the amount of organic carbon of samples.

2.3.4 Electron paramagnetic resonance spectrometer

ROS under irradiation were analyzed using an electron paramagnetic resonance spectrometer (EPR, A300, Bruker). For the radical detection, 20 μL of 0.05 M 5,5-dimethylpyrroline-Noxide (DMPO, in methanol) and 5-tert-butoxycarbonyl-5methyl-1-pyrroline-N-oxide (BMPO, in water) were used as spin traps for superoxide radicals ($•O_2^-$) and •OH, respectively. The parameters were set as follows: magnetic field range of 3450−3550 G, central field range of 3500 G, scan time of 30 s and microwave power of 20 mW.

2.3.5 H_2O_2 detection

The H_2O_2 generation was analyzed by the $TiOSO_4$ colorimetric method (Liu et al., 2023; Li et al., 2023). $TiOSO_4$ reacted with H_2O_2 to form a yellow titanium-peroxide complex ($(Ti(IV)O_2^{2+})$), which exhibited a characteristic absorbance peak at 405 nm. The H_2O_2 concentration was determined using the H_2O_2 standard curve (Fig. S5), and the testing procedure is given in Text S9.

2.3.6 X-ray photoelectron spectroscopy

The X-ray photoelectron spectroscopy (XPS, ESCALAB 250Xi, Thermo) was employed to investigate the valence state variations of metal ions under irradiation. Fresh samples (3 mL, prepared by 2 mL OC extraction with 1 mL ionic solution) or the ones photoaged by SO_2 were combined with SiO_2 (100 mg) and dried by rotary evaporation. Before the XPS analysis, the samples were stored in a vacuum environment to minimize the changes in the valence state of TMIs. Aluminum Kα radiation ($h\nu$ = 1486.68 eV, spot size 500 μm) was used as the excitation source for XPS analysis. The measurements were conducted under ultrahigh vacuum conditions of approximately 10^{-9} mbar. The instrument was operated at 15 kV and 10 mA. Signals were accumulated over 5−10 scans, and the spectra were recorded with a pass energy of 30 eV and a step size of 0.05 eV. Beam-induced effects were assessed by collecting consecutive C 1s spectra at the same sample position. The peak positions and spectral shapes remained consistent, indicating that beam-induced effects were negligible under the measurement conditions. Binding energies were calibrated using the C 1s peak at 284.8 eV. Peak deconvolution was conducted to resolve the contributions of different valence states.

2.3.7 Density functional theory calculations

Molecular structures were constructed in GaussView 6. Density functional theory (DFT) calculations were carried out through the quantum chemistry software Gaussian 16. Geometry optimizations and frequency calculations were performed at the B3LYP/LANL2DZ level. The SMD water solvation model was used to represent aqueous solvation effects. Grimme's D3 dispersion correction was employed to account for van der Waals interactions. All optimized structures were confirmed as local minima without imaginary frequencies. Single-point energy calculations were conducted at the B3LYP/def2-TZVP level using the optimized geometries. O_2 adsorption on OC and the corresponding IGMH diagrams were analyzed using Multiwfn (Lu and Chen, 2011; Lu, 2024). The calculations of complexation energy between OC and TMIs and O_2 adsorption energy are described in Text S10.

3 Results and discussion

3.1 Dependence of SO_2 uptake on metal ions

Fig. 1a−c illustrates the temporal evolution of SO_2 concentration on OC, TMIs and

OC@TMIs under irradiation. All errors denoted the standard deviations of three independent replicates. Because chloride salts were used here, OC@NaCl control experiments were conducted. The decreasing trend of SO_2 concentration on OC@NaCl was the same as that on OC, suggesting no measurable effect of Cl^- on SO_2 uptake (Fig. S6). The SO_2 loss on $FeCl_3$ or $MnCl_2$ was less than that on OC, while it was similar for $CuCl_2$ and OC. When SO_2 was exposed to OC@Fe^{3+}, the SO_2 concentration decreased by 1−2 ppb, which was obviously lower than that for OC+Fe^{3+}. This indicates that the coexistence of Fe^{3+} with OC markedly suppressed the photochemical uptake of SO_2. The SO_2 loss on OC@Cu^{2+} and OC@Mn^{2+} was markedly greater than that on OC+Cu^{2+} and OC+Mn^{2+}, respectively. This suggests that both Cu^{2+} and Mn^{2+} enhanced the photochemical reaction of SO_2 with OC. Dark control experiments showed that SO_2 uptake on OC@TMIs was slightly different from that on OC in the absence of light, indicating that the non-photochemical effects of TMIs to SO_2 uptake was limited (Fig. S7).

The initial (γ_i) and steady-state (γ_{ss}) uptake coefficients of SO_2 are summarized in Fig. 1d. The γ_{ss} was consistently lower than the γ_i due to the gradual aging and the depletion of photoactive components during the reaction. The γ_{ss} on OC@Fe^{3+} only accounted for 5% of that on OC+Fe^{3+}, confirming that Fe^{3+} significantly restrained the photochemical SO_2 uptake on OC. In contrast, γ_{ss} for OC@Cu^{2+} and OC@Mn^{2+} was 1.83 and 2.93 times of the corresponding one for OC+Cu^{2+} and OC+Mn^{2+}, respectively. This definitely suggests that the coexistence of Cu^{2+} and Mn^{2+} with OC has synergistic effects on the photochemical uptake of SO_2, with Mn^{2+} exhibiting a stronger enhancement than Cu^{2+}. Overall, these contrasting behaviors reveal that the addition of TMIs to OC can either restrict (Fe^{3+}) or facilitate (Cu^{2+} and Mn^{2+}) the photochemical uptake of SO_2, highlighting the distinct roles of TMIs in modulating the OC reactivity.

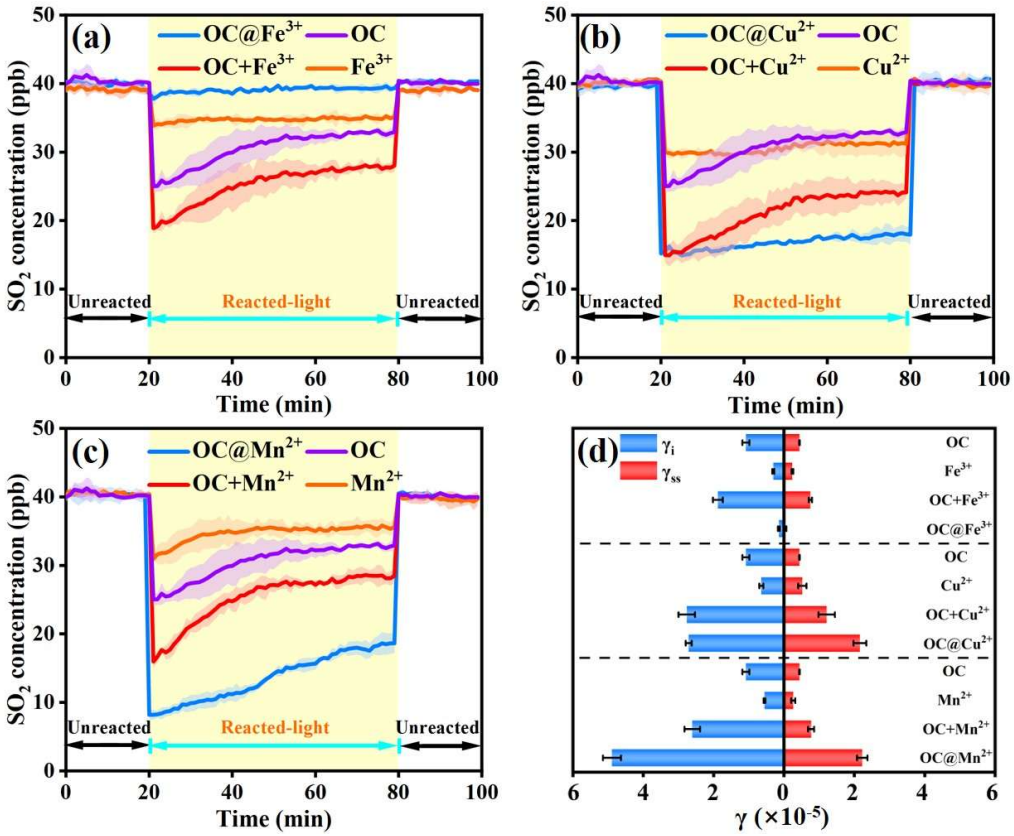

Figure 1. (a−c) Temporal variations of the SO_2 concentration during the heterogeneous reaction of SO_2 with OC, TMIs, OC+TMIs and OC@TMIs under irradiation (For OC+TMIs, SO_2 uptake was the arithmetic sum of that measured for OC and TMIs in the separate experiments). (d) Initial uptake coefficients (γ_i) and steady-state uptake coefficients (γ_{ss}) of SO_2 under irradiation. Reaction conditions: irradiance of 1.05×10^{16} photons cm^{-2} s^{-1}, 40 ppb SO_2, 298 K and 60% RH.

3.2 Dependence of sulfate formation on metal ions

The contour maps of in-situ ATR-IR spectra of OC, TMIs and OC@TMIs exposed to SO_2 under irradiation are displayed in Fig. 2a. Several characteristic sulfate (SO_4^{2-} or HSO_4^-) bands were identified for all samples in the 1300−1000 cm^{-1} region (Zhang et al., 2023; Zhang et al., 2019). It was noted that these bands intensified progressively with the time, reflecting the continuous accumulation of sulfates.

The IC results provided quantitative evidence of sulfate formation under irradiation (Fig. 2b). For OC@Fe^{3+}, sulfate production was much lower than that on OC or $FeCl_3$. Specifically, the sulfate mass on OC@Fe^{3+} was merely 12% of that for OC+Fe^{3+}, confirming that Fe^{3+} restrained

the formation of sulfates on OC. In contrast, the sulfate mass on OC@Cu^{2+} and OC@Mn^{2+} was 1.13 and 1.52 times larger than that for OC+Cu^{2+} and OC+Mn^{2+}, respectively. These confirm that both Cu^{2+} and Mn^{2+} promote the photochemical oxidation of SO_2 to sulfates on OC. Only limited sulfate formation was observed on OC@TMIs under dark conditions, indicating a minor contribution from the non-photochemical pathways (Fig. S8). Taken together with the SO_2 uptake data in Fig.1, TMIs exerted markedly different influences on SO_2 conversion to sulfates on OC.

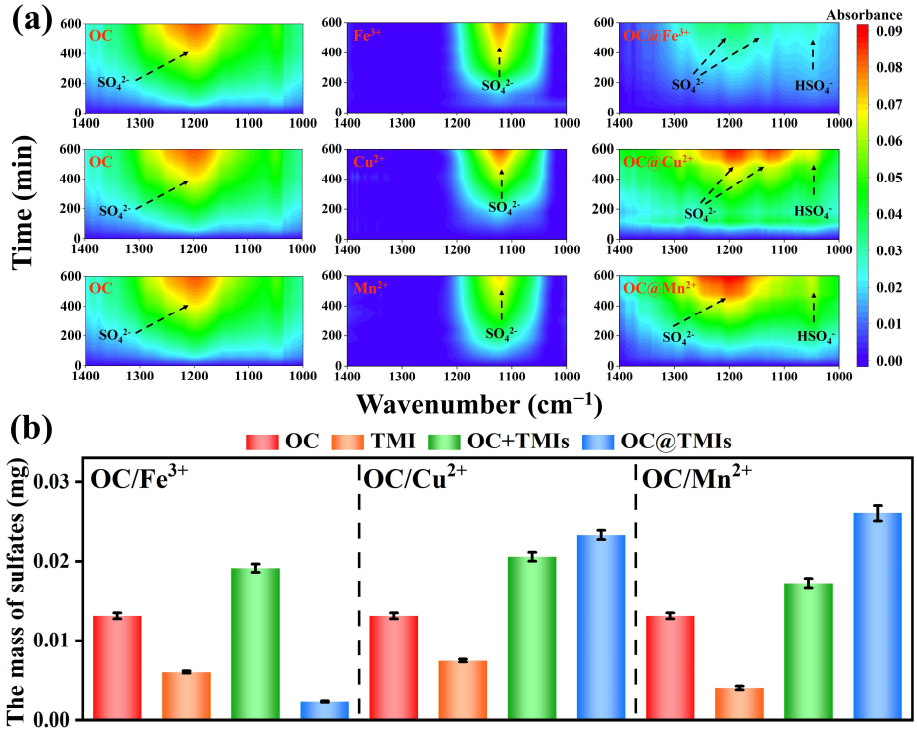

Figure 2. (a) Contour map of in-situ ATR-IR spectra of OC, $FeCl_3$, $CuCl_2$, $MnCl_2$, OC@Fe^{3+}, OC@Cu^{2+} and OC@Mn^{2+} exposed to SO_2 under irradiation. Reaction conditions: irradiance of 7.40×10^{15} photons cm^{-2} s^{-1}, 2 ppm SO_2, 298 K and 60% RH. (b) Mass of sulfates produced on OC, TMIs, OC+TMIs and OC@TMIs after the 10 h reaction with SO_2 under irradiation (For OC+TMIs, its sulfate mass was the arithmetic sum of that measured for OC and TMIs in the separate experiments). Reaction conditions: irradiance of 1.05×10^{16} photons cm^{-2} s^{-1}, 200 ppb SO_2, 298 K and 60% RH.

3.3 Spectroscopic evidence for complexation between OC and TMIs

The complexation between OC and TMIs may occur and alter the optical properties of OC (Wang et al., 2024). Changes in optical absorption and steady-state fluorescence signals were

used to probe these interactions. Fig. S9a−c displays the UV-vis spectra of OC, TMIs, OC+TMIs and OC@TMIs. OC and OC@TMIs exhibited a sharp increase in the absorbance at the shorter wavelengths. $FeCl_3$, $CuCl_2$ and $MnCl_2$ owned very weak absorbance. OC@Fe^{3+}, OC@Cu^{2+} and OC@Mn^{2+} presented lower absorbance than OC+Fe^{3+}, OC+Cu^{2+} and OC+Mn^{2+}, respectively. This decrease in the absorbance suggests the occurrence of interactions between OC and TMIs. The background concentrations of Fe, Mn and Cu in OC were measured by ICP-MS, and they varied in the range of 1.23−7.70 μg L^{-1}. This accounted for only 0.0045%−0.0276% of TMI concentrations used for OC@TMIs. Therefore, the contribution of intrinsic Fe, Mn and Cu to the TMI dependent spectral changes was considered to be very limited. The FT-IR spectra of OC are displayed in Fig. S10, and the peak assignments are summarized in Table S1. OC contained carboxyl, hydroxyl and carbonyl groups. These oxygen-containing groups with π bond electrons and lone pairs can serve as the complexation sites by donating electrons to the vacant orbitals of TMIs (Wang et al., 2021c). Coordination with TMIs can perturb the electronic structure of OC chromophores and affect π-π* or n-π* electronic transitions, which may induce a hypochromic effect in the UV-vis spectra (Qin et al., 2024). To further compare the spectral changes induced by TMIs, differential absorbance was calculated as ΔAbs = Abs(OC+TMIs) − Abs(OC@TMIs). Notably, as shown in Fig. S9d, there was the largest ΔAbs between OC@Fe^{3+} and OC+Fe^{3+} in the entire spectral range, indicating the strongest complexation of OC with Fe^{3+} among three TMIs.

EEM fluorescence spectroscopy combining with the PARAFAC analysis were employed to further investigate the complexation interactions between TMIs on OC. Three chromophores are identified in Fig. 3a−c and Fig. S11, and their peak positions and assignments are given in Table S2. C1 (Ex/Em = 265(320)/380 nm) and C2 (Ex/Em = 285(370)/420 nm) were assigned to chromophores with low and high oxidation states, respectively. C3 (Ex/Em = 200(260)/340 nm) belonged to protein-like chromophores (Li et al., 2022; Wang et al., 2021b). Fluorophores at longer emission wavelengths, such as C2, typically owned abundant polar groups, including hydroxyl and carboxyl, which acted as primary binding sites for TMIs (Pan et al., 2020; Lu et al., 2019). The relative contributions of different components to OC shifted upon the addition of TMIs (Fig. 3d), reflecting the varied complexation strengths of TMIs with OC (Ma et al., 2022; Yan and Korshin, 2014). For OC@Fe^{3+} in comparison with OC, the ratio of C1 obviously

increased by 14%, while it decreased by 9% and 5% for C2 and C3, respectively. By contrast, OC@Cu^{2+} and OC@Mn^{2+} showed smaller changes in the C1−C3 proportions. These mean that Fe^{3+} forms the most stable complexes with OC due to its high charge density and trivalent oxidation state, which would enhance the ligand attraction and enable higher coordination numbers (Liu et al., 2022). Cu^{2+} and Mn^{2+}, with lower charge densities and less favorable coordination geometries, exerted weaker complexation effects with OC.

As a comprehensive measure of fluorescence intensity, the total fluorescence volume (TFV) was used to evaluate the overall impact of metal complexations (Fig. 3e). The addition of TMIs led to a reduction in TFV, confirming the fluorescence quenching occurrence. Fe^{3+} caused the most pronounced reduction of TFV (85.2%), followed by Cu^{2+} (13.4%) and Mn^{2+} (1.4%). This strong quenching effect was attributed to the high binding affinity of Fe^{3+} with highly oxidative and protein-like fluorophores. The complexation between OC and TMIs can disrupt the π–π^* conjugation and deactivate fluorescence centers, which contributed to a significant reduction in TFV (Kuramochi et al., 2018). In addition, the complexation of Fe^{3+} with OC could promote the intersystem crossing (ISC) from the singlet state ($^1OC^*$) to the triplet state ($^3OC^*$) (Ruzi et al., 2017; Treacy and Rovis, 2024), enhancing nonradiative decay and further suppressing the fluorescence emission.

To directly demonstrate the complexation strength between TMIs with species in OC, DFT calculations were conducted using Phenol (PH), benzoic acid (BA) and a model substance (MS) (Fig. S12). PH and BA were chosen according to FT-IR analysis (Fig. S10), as they represented species with hydroxyl and carboxyl groups commonly present in OC. MS simultaneously contained these functional groups with a π-conjugated aromatic backbone to better reflect the structural features of ambient OC. Text S11 and Fig. S13 illustrate the complexation structure of three molecular models with Fe^{3+}, Cu^{2+} and Mn^{2+}. As summarized in Table S3, all molecular models exhibited the strongest complexation energy with Fe^{3+}, followed by Cu^{2+} and Mn^{2+}. This was well consistent with the results observed in the UV-vis and fluorescence spectra. Although these models cannot capture the full molecular heterogeneity of OC, the consistency between the calculated results and experimental trends helped to understand the complexation effects of OC with TMIs. Complexation strength is commonly described using stability constants (log K). Because OC was a heterogeneous mixture with multiple potential binding

sites, log K may not be exactly determined. Weak and strong complexation described here was relative sense, according to UV-vis spectral change, fluorescence quenching and complexation energy.

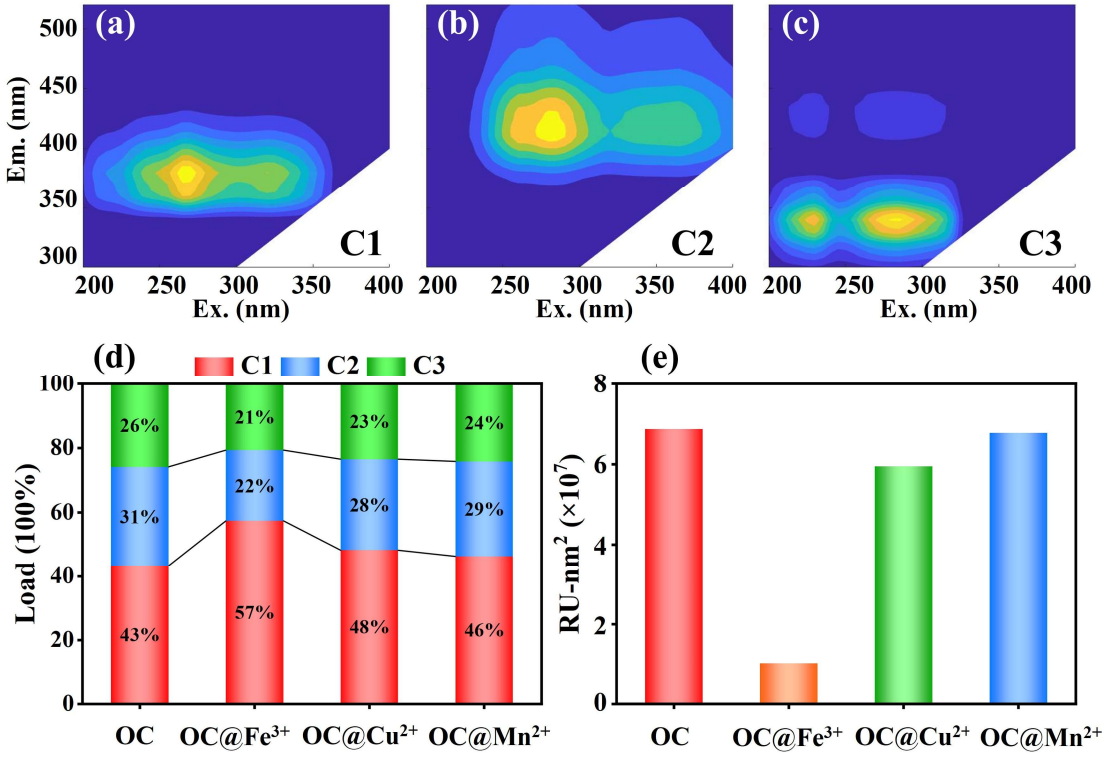

Figure 3. (a−c) Three components extracted by the PARAFAC analysis. (d) Relative fluorescence contributions of C1−C3 in OC, OC@Fe^{3+}, OC@Cu^{2+} and OC@Mn^{2+}. (e) Total fluorescence volume of OC, OC@Fe^{3+}, OC@Cu^{2+} and OC@Mn^{2+}.

3.4 Mechanistic insights into TMIs-regulated oxidation of SO_2 to sulfates

As described through R1−6, previous studies have proposed the photochemical conversion pathways of SO_2 to sulfates on OC (Yang et al., 2025; Yang et al., 2024a). Upon accepting photons, OC is excited to $^3OC^*$, which subsequently generates free electrons (R1−2) (Yang et al., 2024a; Wang et al., 2020). These electrons would reduce adsorbed O_2 to $\bullet O_2^-$ (R3) (Zhang et al., 2022). $\bullet O_2^-$ can combine with protons to form hydroperoxyl radicals ($HO_2^\bullet$), which are converted into O_2 and hydrogen peroxide (H_2O_2) (R4) (Zhang et al., 2020c). H_2O_2 undergoes the photolysis to produce •OH (R5), and •OH drives the oxidation of adsorbed SO_2 or H_2SO_3 or HSO_3^- to sulfates (R6) (Liu et al., 2020b).

$$OC \xrightarrow{h\nu} {}^3OC^* \quad (R1)$$

$$^3OC^* \rightarrow OC^+ + e^- \quad (R2)$$

$$O_2 + e^- \rightarrow \bullet O_2^- \quad (R3)$$

$$\bullet O_2^- + H^+ \rightarrow HO_2^\bullet \rightarrow O_2 + H_2O_2 \quad (R4)$$

$$H_2O_2 \xrightarrow{h\nu} \bullet OH \quad (R5)$$

$$\bullet OH + SO_2 \text{ or } H_2SO_3\ (HSO_3^-) \rightarrow SO_4^{2-} + H_2O \quad (R6)$$

To verify whether the above mechanism remained operative after the complexation between TMIs and OC, electrochemical and EPR analyses were conducted. Mediated electrochemical oxidation (MEO) data of OC without or with TMIs showed persistent occurrence of the photo-generated electron transfer (Fig. S14 and S15). BMPO was used as the spin-trapping agent. As displayed in Fig. 4a, the characteristic EPR signal of BMPO-•OH adducts was detected under irradiation, confirming the generation of •OH. Moreover, EPR signals of BMPO-•OH adducts followed the order: OC@Mn^{2+} > OC@Cu^{2+} > OC > OC@Fe^{3+}, which well aligned with γ_{ss} and sulfate production. The critical role of •OH in the conversion of SO_2 to sulfates was further determined using $NaHCO_3$ to scavenge •OH (Yang et al., 2024a), where the sulfate formation was markedly restricted (Fig. S17). These demonstrate that •OH generation capacity is the primary determinant of sulfate formation on OC@TMIs.

According to the reactions R1−2, the photogeneration of electrons was an initial step that can affect the reaction activity of OC. Fig. 4b summarizes the distinct regulatory roles of Fe^{3+}, Cu^{2+} and Mn^{2+} in the EDC of OC under irradiation. The EDC of OC@Fe^{3+} (0.00496 μmol e^- (mg C)$^{-1}$) was substantially less than that of OC+Fe^{3+} (0.01904 μmol e^- (mg C)$^{-1}$), suggesting that Fe^{3+} significantly suppressed the photogeneration of electrons. This mainly stemmed from the strong complexation of Fe^{3+} and OC, which masked the redox-active moieties and dynamically quenched $^3OC^*$, restraining free electron formation (Li et al., 2022; Liu et al., 2024). Fig. 4b shows that EDC of OC@Cu^{2+} (0.02074 μmol e^- (mg C)$^{-1}$) and OC@Mn^{2+} (0.02147 μmol e^- (mg C)$^{-1}$) was higher than that of OC+Cu^{2+} (0.01959 μmol e^- (mg C)$^{-1}$) and OC+Mn^{2+} (0.01812 μmol e^- (mg C)$^{-1}$), respectively. This means that Cu^{2+} and Mn^{2+} enhance the electron-donating ability of OC. These larger EDC may be related to reversible redox cycling of Cu^{2+}/Cu^+ and Mn^{2+}/Mn^{3+} in the photochemical process. In contrast, Fe^{3+} formed more stable complexes with OC that trapped the photogenerated electrons, thereby suppressing

efficient redox cycling of Fe^{3+}/Fe^{2+}. Under irradiation, Cu^{2+} was reduced to Cu^{+} by accepting photogenerated electrons, which was subsequently re-oxidized to Cu^{2+} by O_2 or electron-deficient functional groups (e.g., quinones) (Pan et al., 2020). As displayed in XPS spectra of Cu 2p for OC@Cu^{2+} in Fig. 4c and d, the peaks at 932.5 and 934.3 eV corresponded to Cu^{+} and Cu^{2+}, respectively (Biesinger et al., 2011). The proportion of Cu^{2+}, denoted as R(Cu^{2+}), decreased from 0.67 to 0.59 after photochemical SO_2 aging. This confirms the existence of reversible redox cycling of Cu^{2+}/Cu^{+}. Similarly, Mn^{2+} can be oxidized to Mn^{3+} by photogenerated holes (OC^{+}) or reactive oxygen-containing intermediates on OC, and then Mn^{3+} was reduced by phenolic or aromatic groups on OC (Hansard et al., 2011). The Mn $2p_{3/2}$ spectra of OC@Mn^{2+} exhibited two peaks at 640.4 and 641.9 eV (Fig. 4e and f), which were ascribed to Mn^{2+} and Mn^{3+}, respectively (Cerrato et al, 2010; Xing et al., 2025). The proportion of Mn^{2+} (R(Mn^{2+})) decreased from 0.41 to 0.16 after the reaction, indicating Mn^{2+}/Mn^{3+} redox interconversion. These reversible redox cycles facilitated dynamic interfacial electron transfer by accepting and releasing photogenerated electrons. This bidirectional electron flow can amplify the outward electron flux from OC, thereby increasing the electron-donating capacity (Fulda et al., 2013; Li et al., 2021).

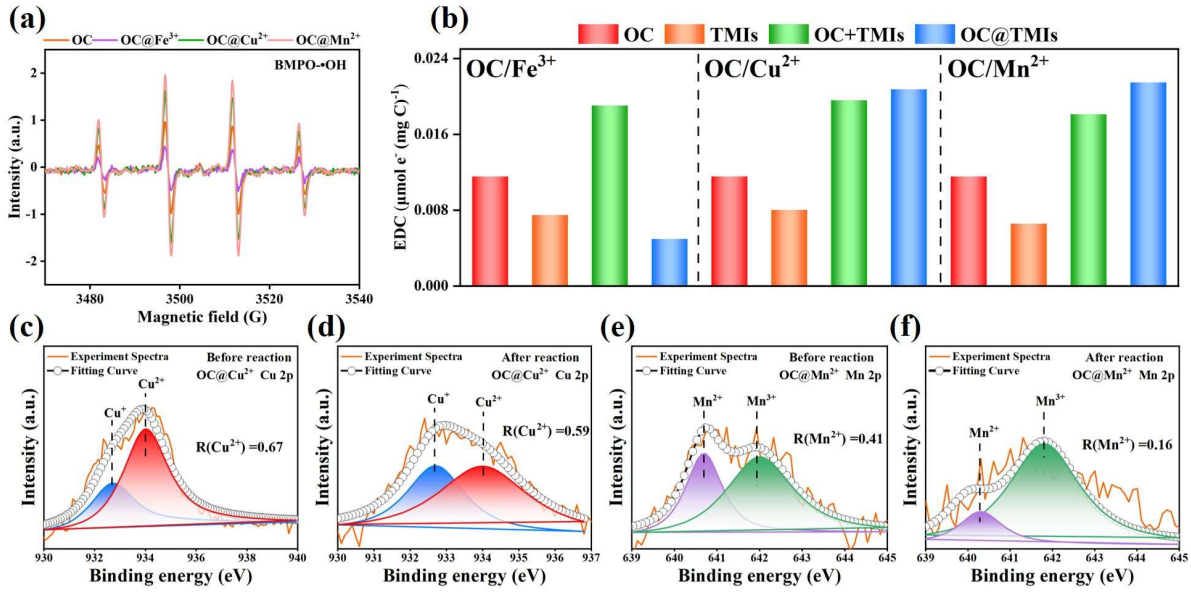

Figure 4. (a) BMPO-•OH adduct EPR spectra of OC, OC@Fe^{3+}, OC@Cu^{2+} and OC@Mn^{2+} under irradiation. (b) Electron donating capacity (EDC) of OC, TMIs, OC+TMIs and OC@TMIs (For OC+TMIs, EDC was the arithmetic sum of that measured for OC and TMIs in separate experiments). High-resolution XPS spectra of Cu 2p for OC@Cu^{2+} (c) before and

(d) after the reaction, and Mn 2p for OC@Mn^{2+} (e) before and (f) after the reaction (R(Cu^{2+}) and R(Mn^{2+}) denoted the proportion of Cu^{2+} and Mn^{2+} on the surface, respectively).

As shown in the reaction R3, $\bullet O_2^-$ formation relied not only on the photogenerated electrons but also on the O_2 activation. To elucidate the effect of TMIs complexation on the O_2 activation, DFT calculations were carried out in the interaction of O_2 with MS (Fig. S18). Fig. 5a displays that O_2 adsorption energy on MS was −82.03 kJ mol^{-1}, with O−O bond length of 1.20 Å. For MS@Fe^{3+}, O_2 adsorption energy became more negative (−205.59 kJ mol^{-1}), reflecting stronger electrostatic binding due to high positive charge of metal center (Zhang et al., 2024). However, O−O bond length remained unchanged, suggesting negligible electron transfer into the π* antibonding orbital of O_2. Thus, O_2 is strongly bound yet not appreciably activated. Complexation between OC with Cu^{2+} or Mn^{2+} obviously enhanced the adsorption of O_2 (−212.93 kJ mol^{-1} for Cu^{2+} and −366.32 kJ mol^{-1} for Mn^{2+}). The O−O bond length slightly increased to 1.21 Å for MS@Cu^{2+}, while it was markedly elongated to 1.32 Å for MS@Mn^{2+}. These changes suggest electron transfer from the metal centers to the π* antibonding orbital of O_2, boosting effective activation of O_2 and facilitating the $\bullet O_2^-$ generation. Compared to Cu^{2+}, Mn^{2+} exhibited stronger O_2 activation, which was attributed to its half-filled $3d^5$ configuration and moderate redox potential, both of which favored efficient π* electron donation.

Accordingly, Fe^{3+} inhibited electron generation and failed to activate O_2, whereas Cu^{2+} and Mn^{2+} promoted these two processes, with Mn^{2+} showing a stronger enhancement effect. This led to the $\bullet O_2^-$ signal intensity order of OC@Mn^{2+} > OC@Cu^{2+} > OC > OC@Fe^{3+} (Fig. 5b). $\bullet O_2^-$ directly contributed to H_2O_2 formation (R4), which was quantified with a $TiOSO_4$ chromogenic method (Fig. S20). Fig. 5c shows that H_2O_2 production trend had the consistency with •OH generation ability among these samples (Fig. 4a), which ultimately governed the photoconversion of SO_2 to sulfates.

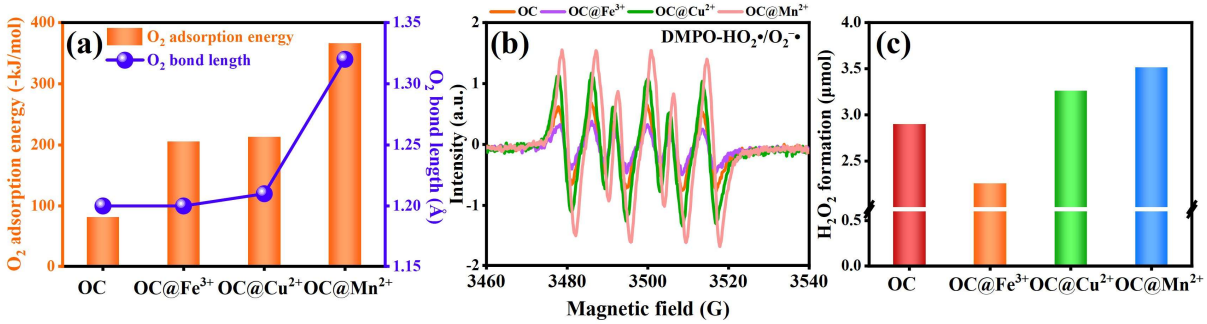

Figure 5. (a) O_2 adsorption energy and the bond length of O_2 for MS, MS@Fe^{3+}, MS@Cu^{2+} and MS@Mn^{2+}. (b) EPR spectra of DMPO-$HO_2^{\bullet}$/$\bullet O_2^-$ adduct for OC, OC@Fe^{3+}, OC@Cu^{2+} and OC@Mn^{2+} under irradiation. (c) H_2O_2 formation from the photochemical reactions on OC, OC@Fe^{3+}, OC@Cu^{2+} and OC@Mn^{2+}.

3.5 Discussion

The OC samples were collected from smoke aerosols generated during coal combustion. The TMIs concentrations selected here were atmospherically relevant soluble metal ion levels. These systems may roughly represent the coexistence of OC and TMIs for atmospheric aerosols in polluted regions affected by coal combustion emissions. High humidity and acidic conditions may promote metal dissolution and facilitate the complexation between soluble metal ions and OC. The photochemical lifetime of SO_2 (τ_{SO_2}) on OC@TMIs was calculated with Eq. (2) (Yang et al., 2021),

$$\tau_{SO_2} = \frac{4}{\gamma \nu A} \quad (2)$$

where γ represents the uptake coefficient of SO_2; ν denotes the mean SO_2 molecular velocity; A corresponds to the aerosol surface area concentration. Based on field measurements during heavily polluted episodes, A ranged from 5.44×10^{-5} to 8.16×10^{-5} cm^2 cm^{-3} (Zhang et al., 2018; Yang et al., 2021). Under typical atmospheric conditions (40 ppb SO_2, 60% RH), γ_{ss} for SO_2 on OC@TMIs were determined to be $(0.39-22.24) \times 10^{-6}$. Organic matters typically account for approximately 20%–45% of $PM_{2.5}$ mass (Wu et al., 2018). The τ_{SO_2} was estimated to be 1.8–379 days in the coexistence of OC and TMIs. By contrast, τ_{SO_2} on OC from coal combustion was much narrower, which ranged from 17 to 53 days under the same conditions (Yang et al., 2025).

To assess the atmospheric production of sulfates during the photooxidation of SO_2 on

OC@TMIs, the sulfate formation rate (R) was estimated using Eq. (3),

$$R = \frac{d[SO_4^{2-}]}{dt} = \left[\frac{R_P}{D_g} + \frac{4}{\gamma v}\right]^{-1} A\,[SO_2] \quad (3)$$

where D_g refers to the diffusion coefficient of SO_2 (1.12×10^{-5} m^2 s^{-1}); R_P denotes the aerosol particle radius and is estimated via Eq. (4) (Li et al., 2020),

$$R_P = \left(0.254 \times \frac{[PM_{2.5}]}{(\mu g\, m^{-3})} + 10.259\right) \times 10^{-9} \quad (4)$$

where $[PM_{2.5}]$ denotes the mean mass concentration of $PM_{2.5}$, and a concentration range of 100−500 μg m^{-3} for the polluted episodes in typical Chinese cities was adopted here (Chu et al., 2020). Under these conditions, R was determined to be 0.07−5.95 μg m^{-3} h^{-1}, which was a substantially broader range than 0.43−1.33 μg m^{-3} h^{-1} for OC (Yang et al., 2025). Broader ranges of τ_{SO_2} and R on OC@TMIs indicate that the coexistence of OC and TMIs significantly modulates the photochemical conversion of SO_2 to sulfates. These findings suggest that current model simulations may underestimate or overestimate sulfate formation on OC by overlooking such antagonistic or synergistic processes.

It has been well demonstrated that •OH was the dominant active species responsible for the oxidation of SO_2 to sulfates on OC@TMIs (Fig. 4 and S17). Other metal ions (Ca^{2+}, Co^{2+}, Zn^{2+}, Mg^{2+}, Ni^{2+}, Cr^{3+} and Al^{3+}) commonly presenting in atmospheric aerosols were expanded to examine whether this mechanism exhibited broader generality (Hua et al., 2024). As shown in Fig. 6a, the peaks of BMPO-•OH adducts were observed under irradiation, confirming the •OH generation on all OC@TMIs. Relative to OC, the coexistence of Ca^{2+}, Co^{2+}, Zn^{2+} and Mg^{2+} obviously promoted the •OH generation, while Ni^{2+}, Cr^{3+} and Al^{3+} exerted an inhibitory effect. Fig. S21 summarized the mass of sulfates formed on OC@TMIs, which was consistent with the •OH generation trend. Importantly, a linearly positive relationship ($R^2 = 0.97$) between •OH intensity and sulfate mass ($M_{sulfates}$) was determined in Fig. 6b. $M_{sulfates}$ can be parametrized as a function of •OH signal intensity (I) with an Eq.: $M_{sulfates} = (1.68 \pm 0.11) \times 10^{-2} \times I - (0.43 \pm 0.08) \times 10^{-2}$. The linear relationship between •OH intensity and sulfate formation was established using fresh OC from coal combustion and different TMIs at the same concentration. OC in aerosols generally stems from diverse sources and undergoes the atmospheric aging processes, which would significantly modify the compositions and structures of OC (Cao et al.,

2021; Deng et al., 2022). TMIs types and concentrations also display temporal and spatial variations (Ito et al., 2016; Moreno et al., 2011). These may alter the complexation between OC and TMIs and consequently affect •OH generation and sulfate formation. Thus, there may be some uncertainties for the applicability of this linear relationship under ambient conditions. Nevertheless, this quantitative relationship highlighted the potential dual roles of metal ion types in the sulfate formation, challenging the traditional view that metal ions often promote the SO_2 oxidation (Cao et al., 2024a; Wang et al., 2022; Wang et al., 2021a). It also emphasized the critical role of •OH in the sulfate formation on OC@TMIs. Accordingly, incorporating the •OH generation ability of diverse OC@TMIs complexes into the atmospheric models may help to constrain sulfate source strength, predict haze evolution and assess associated health impacts in polluted environments.

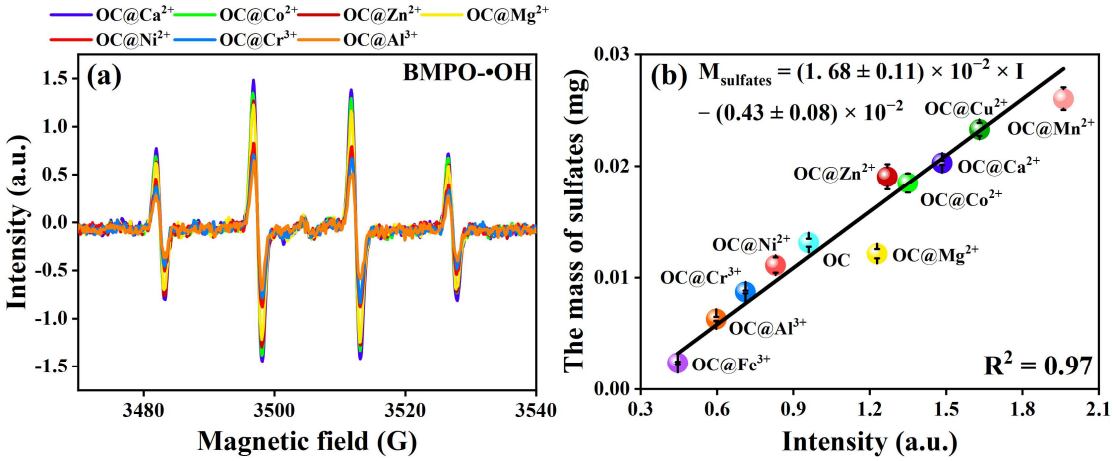

Figure 6. (a) BMPO-•OH adduct EPR spectra under irradiation. (b) The correlation of $M_{sulfates}$ with the generation of •OH.

4 Conclusions

It was well confirmed that the heterogeneous photooxidation of SO_2 to sulfates was strongly modulated by the interactions of OC with TMIs. As evidenced by SO_2 uptake coefficient and sulfate formation mass, Fe^{3+} exhibited a significantly inhibitory effect, whereas Cu^{2+} and Mn^{2+} promoted the conversion of SO_2 to sulfates, with Mn^{2+} playing a more obvious enhancement role. Spectroscopic analyses and DFT calculations consistently demonstrated that Fe^{3+} had the strongest binding affinity to OC chromophores, followed by Cu^{2+} and Mn^{2+}. This difference in the complexation strength controlled the electron generation, O_2 activation, and the sequential formation of $•O_2^-$, H_2O_2, and •OH. In particular, a quantitative linear correlation was

established between •OH intensity and sulfate mass across a wide range of metal ions. This clearly suggests that the regulation of sulfate formation on OC by metal ions is dominated by their capacity to suppress or enhance •OH generation.

Data availability. The data used in this study are available from the corresponding author upon request (hanch@smm.neu.edu.cn).

Supplement. Figures, texts and tables about experimental section, SO_2 uptake and sulfate formation, complexation evidences of OC with metal ions, the mechanism verification and discussion.

Author contributions. CH and SY designed the experiment; SY and SL conducted the experiments; SY, SL, JZ, HN, FL and WY performed the data interpretation; CH and SY wrote the paper. CH supervised the project.

Competing interests. The contact author has declared that none of the authors has any competing interests.

Financial support. This work has been supported by the National Natural Science Foundation of China (grant nos. 42575113, 42577113, 42077198 and 22206023), and the Fundamental Research Funds for the Central Universities (grant nos. N25GFZ016 and N26BSS035). The characterization analysis of this work was supported by the Analytical and Testing Center of Northeastern University, China.

References

Biesinger, M. C., Payne, B. P., Grosvenor, A. P., Lau, L. W. M., Gerson, A. R., and Smart, R. S. C.: Resolving surface chemical states in XPS analysis of first row transition metals, oxides and hydroxides: Cr, Mn, Fe, Co and Ni, Appl. Surf. Sci., 257, 2717−2730, https://doi.org/10.1016/j.apsusc.2010.10.051, 2011.

Cao, T., Li, M., Zou, C., Fan, X., Song, J., Jia, W., Yu, C., Yu, Z., and Peng, P. a.: Chemical composition, optical properties, and oxidative potential of water- and methanol-soluble organic compounds emitted from the combustion of biomass materials and coal, Atmos.

Chem. Phys., 21, 13187−13205, https://doi.org/10.5194/acp-21-13187-2021, 2021.

Cao, X., Liu, Y.-X., Huang, Q., Chen, Z., Sun, J., Sun, J., Pang, S.-F., Liu, P., Wang, W., Zhang, Y.-H., and Ge, M.: Single droplet tweezer revealing the reaction mechanism of Mn(II)-catalyzed SO_2 oxidation, Environ. Sci. Technol., 58, 5068−5078, https://doi.org/10.1021/acs.est.4c00309, 2024a.

Cao, Y., Liu, J., Ma, Q., Zhang, C., Zhang, P., Chen, T., Wang, Y., Chu, B., Zhang, X., Francisco, J. S., and He, H.: Photoactivation of chlorine and its catalytic role in the formation of sulfate aerosols, J. Am. Chem. Soc., 146, 1467−1475, https://doi.org/10.1021/jacs.3c10840, 2024b.

Cerrato, J. M., Hochella, M. F., Jr., Knocke, W. R., Dietrich, A. M., and Cromer, T. F.: Use of XPS to identify the oxidation state of Mn in solid surfaces of filtration media oxide samples from drinking water treatment plants, Environ. Sci. Technol., 44, 5881−5886, https://doi.org/10.1021/es100547q, 2010.

Chu, B., Ma, Q., Liu, J., Ma, J., Zhang, P., Chen, T., Feng, Q., Wang, C., Yang, N., Ma, H., Ma, J., Russell, A. G., and He, H.: Air pollutant correlations in China: Secondary air pollutant responses to NO_x and SO_2 control, Environ. Sci. Technol. Lett., 7, 695−700, https://doi.org/10.1021/acs.estlett.0c00403, 2020.

Deng, J., Ma, H., Wang, X., Zhong, S., Zhang, Z., Zhu, J., Fan, Y., Hu, W., Wu, L., Li, X., Ren, L., Pavuluri, C. M., Pan, X., Sun, Y., Wang, Z., Kawamura, K., and Fu, P.: Measurement report: Optical properties and sources of water-soluble brown carbon in Tianjin, North China-insights from organic molecular compositions, Atmos. Chem. Phys. 22, 6449−6470, https://doi.org/10.5194/acp-22-6449-2022, 2022.

Dupart, Y., King, S. M., Nekat, B., Nowak, A., Wiedensohler, A., Herrmann, H., David, G., Thomas, B., Miffre, A., Rairoux, P., D'Anna, B., and George, C.: Mineral dust photochemistry induces nucleation events in the presence of SO_2, P. Natl. Acad. Sci. USA, 109, 20842−20847, https://doi.org/10.1073/pnas.1212297109, 2012.

Eckhardt, S., Quennehen, B., Olivié, D. J. L., Berntsen, T. K., Cherian, R., Christensen, J. H., Collins, W., Crepinsek, S., Daskalakis, N., Flanner, M., Herber, A., Heyes, C., Hodnebrog, Ø., Huang, L., Kanakidou, M., Klimont, Z., Langner, J., Law, K. S., Lund, M. T., Mahmood, R., Massling, A., Myriokefalitakis, S., Nielsen, I. E., Nøjgaard, J. K., Quaas, J., Quinn, P. K., Raut, J. C., Rumbold, S. T., Schulz, M., Sharma, S., Skeie, R. B., Skov, H., Uttal, T., von

Salzen, K., and Stohl, A.: Current model capabilities for simulating black carbon and sulfate concentrations in the Arctic atmosphere: A multi-model evaluation using a comprehensive measurement data set, Atmos. Chem. Phys., 15, 9413−9433, https://doi.org/10.5194/acp-15-9413-2015, 2015.

Fan, X., Wei, S., Zhu, M., Song, J., and Peng, P. A.: Comprehensive characterization of humic-like substances in smoke $PM_{2.5}$ emitted from the combustion of biomass materials and fossil fuels, Atmos. Chem. Phys., 16, 13321−13340, https://doi.org/10.5194/acp-16-13321-2016, 2016.

Fulda, B., Voegelin, A., Maurer, F., Christl, I., and Kretzschmar, R.: Copper redox transformation and complexation by reduced and oxidized soil humic acid. 1. X-ray absorption spectroscopy study, Environ. Sci. Technol., 47, 10903−10911, https://doi.org/10.1021/es4024089, 2013.

Hansard, S. P., Easter, H. D., and Voelker, B. M.: Rapid reaction of nanomolar Mn(II) with superoxide radical in seawater and simulated freshwater, Environ. Sci. Technol., 45, 2811−2817, https://doi.org/10.1021/es104014s, 2011.

Hoyle, C. R., Fuchs, C., Järvinen, E., Saathoff, H., Dias, A., El Haddad, I., Gysel, M., Coburn, S. C., Tröstl, J., Bernhammer, A. K., Bianchi, F., Breitenlechner, M., Corbin, J. C., Craven, J., Donahue, N. M., Duplissy, J., Ehrhart, S., Frege, C., Gordon, H., Höppel, N., Heinritzi, M., Kristensen, T. B., Molteni, U., Nichman, L., Pinterich, T., Prévôt, A. S. H., Simon, M., Slowik, J. G., Steiner, G., Tomé, A., Vogel, A. L., Volkamer, R., Wagner, A. C., Wagner, R., Wexler, A. S., Williamson, C., Winkler, P. M., Yan, C., Amorim, A., Dommen, J., Curtius, J., Gallagher, M. W., Flagan, R. C., Hansel, A., Kirkby, J., Kulmala, M., Möhler, O., Stratmann, F., Worsnop, D. R., and Baltensperger, U.: Aqueous phase oxidation of sulphur dioxide by ozone in cloud droplets, Atmos. Chem. Phys., 16, 1693−1712, https://doi.org/10.5194/acp-16-1693-2016, 2016.

Hua, C., Ma, W., Zheng, F., Zhang, Y., Xie, J., Ma, L., Song, B., Yan, C., Li, H., Liu, Z., Liu, Q., Kulmala, M., and Liu, Y.: Health risks and sources of trace elements and black carbon in $PM_{2.5}$ from 2019 to 2021 in Beijing, J. Environ. Sci., 142, 69−82, https://doi.org/10.1016/j.jes.2023.05.023, 2024.

Hua, C., Ma, W., Li, J., Wang, Y., Zheng, F., Zhang, Y., Ren, Y., Chen, T., Li, H., Bianchi, F.,

564 Petaja, T., Kerminen, V. M., Worsnop, D., Kulmala, M., Kan, H., and Liu, Y.: Internal
565 exposure risks of particle-bound polycyclic aromatic hydrocarbons with an hourly time
566 resolution to humans in Beijing, Environ. Sci. Technol., 59, 12035−12047,
567 https://doi.org/10.1021/acs.est.5c00578, 2025.
568 Huang, R.-J., Zhang, Y., Bozzetti, C., Ho, K.-F., Cao, J.-J., Han, Y., Daellenbach, K. R., Slowik,
569 J. G., Platt, S. M., Canonaco, F., Zotter, P., Wolf, R., Pieber, S. M., Bruns, E. A., Crippa, M.,
570 Ciarelli, G., Piazzalunga, A., Schwikowski, M., Abbaszade, G., Schnelle-Kreis, J.,
571 Zimmermann, R., An, Z., Szidat, S., Baltensperger, U., Haddad, I. E., and Prévôt, A. S. H.:
572 High secondary aerosol contribution to particulate pollution during haze events in China,
573 Nature, 514, 218−222, https://doi.org/10.1038/nature13774, 2014.
574 Ito, K., Johnson, S., Kheirbek, I., Clougherty, J., Pezeshki, G., Ross, Z., Eisl, H., and Matte, T.
575 D.: Intraurban variation of fine particle elemental concentrations in New York city, Environ.
576 Sci. Technol., 50, 7517−7526, https://doi.org/10.1021/acs.est.6b00599, 2016.
577 Jiang, S.-d., Wang, Z.-h., Zhou, J.-h., Wen, Z.-c., and Cen, K.-f.: A quantum chemistry study
578 on reaction mechanisms of SO_2 with O_3 and H_2O_2, J. Zhejiang Univ-Sci. A, 10, 1327−1333,
579 https://doi.org/10.1631/jzus.A0820787, 2009.
580 Kuramochi, Y., Ishitani, O., and Ishida, H.: Reaction mechanisms of catalytic photochemical
581 CO_2 reduction using Re(I) and Ru(II) complexes, Coord. Chem. Rev., 373, 333−356,
582 https://doi.org/10.1016/j.ccr.2017.11.023, 2018.
583 Li, G., Bei, N., Cao, J., Huang, R., Wu, J., Feng, T., Wang, Y., Liu, S., Zhang, Q., Tie, X., and
584 Molina, L. T.: A possible pathway for rapid growth of sulfate during haze days in China,
585 Atmos. Chem. Phys., 17, 3301−3316, https://doi.org/10.5194/acp-17-3301-2017, 2017.
586 Li, H., Santos, F., Butler, K., and Herndon, E.: A critical review on the multiple roles of
587 manganese in stabilizing and destabilizing soil organic matter, Environ. Sci. Technol., 55,
588 12136−12152, https://doi.org/10.1021/acs.est.1c00299, 2021.
589 Li, H., Yang, K., Hai, L., Wang, Z., Luo, Y., He, L., Yi, W., Li, J., Xu, C., Deng, L., and He, D.:
590 Photothermal-triggered release of alkyl radicals and cascade generation of hydroxyl radicals
591 via a versatile hybrid nanocatalyst for hypoxia-irrelevant synergistic antibiofilm therapy,
592 Chem. Eng. J., 455, 140903, https://doi.org/10.1016/j.cej.2022.140903, 2023.
593 Li, J., Chen, Q., Sha, T., and Liu, Y.: Significant promotion of light absorption ability and

formation of triplet organics and reactive oxygen species in atmospheric HULIS by Fe(III) ions, Environ. Sci. Technol., 56, 16652−16664, https://doi.org/10.1021/acs.est.2c05137, 2022.

Li, J., Zhang, Y.-L., Cao, F., Zhang, W., Fan, M., Lee, X., and Michalski, G.: Stable sulfur isotopes revealed a major role of transition-metal ion-catalyzed SO_2 oxidation in haze episodes, Environ. Sci. Technol., 54, 2626−2634, https://doi.org/10.1021/acs.est.9b07150, 2020.

Liu, J., Li, X., Chu, Y., Yuan, L., Lv, R., and Zhang, W.: An autocatalytic Fe(III)/H_2O_2 Fenton-like process triggered by tetracycline: The overlooked effect of quinone intermediates, Chem. Eng. J., 475, 146035, https://doi.org/10.1016/j.cej.2023.146035, 2023.

Liu, P., Liu, Y.-X., Huang, Q., Chao, X., Zhong, M., Yin, J., Zhang, X., Li, L.-F., Kang, X.-Y., Chen, Z., Pang, S., Wang, W., Zhang, Y.-H., and Ge, M.: Sulfate formation through copper-catalyzed SO_2 oxidation by NO_2 at aerosol surfaces, npj Clim. Atmos. Sci., 8, 57, https://doi.org/10.1038/s41612-025-00934-z, 2025.

Liu, T. and Abbatt, J. P. D.: Oxidation of sulfur dioxide by nitrogen dioxide accelerated at the interface of deliquesced aerosol particles, Nat. Chem., 13, 1173−1177, https://doi.org/10.1038/s41557-021-00777-0, 2021.

Liu, T., Clegg, S. L., and Abbatt, J. P. D.: Fast oxidation of sulfur dioxide by hydrogen peroxide in deliquesced aerosol particles, P. Natl. Acad. Sci. USA, 117, 1354−1359, https://doi.org/10.1073/pnas.1916401117, 2020a.

Liu, X., Lu, J., Fang, X., Zhou, J., and Chen, Q.: Complexation modelling and oxidation mechanism of organic pollutants in cotton pulp black liquor during iron salt precipitation and electrochemical treatment, Chemosphere, 308, 136374, https://doi.org/10.1016/j.chemosphere.2022.136374, 2022.

Liu, Y., Zhao, W., Zhang, P., Fu, Q.-l., Yu, C., and Yuan, S.: Asymmetrical changes of electron-donating and electron-accepting capacities of natural organic matter during its interaction with Fe oxyhydroxides, Chem. Geol., 661, 122189, https://doi.org/10.1016/j.chemgeo.2024.122189, 2024.

Liu, Y., Wang, T., Fang, X., Deng, Y., Cheng, H., Bacha, A.-U.-R., Nabi, I., and Zhang, L.: Brown carbon: An underlying driving force for rapid atmospheric sulfate formation and haze

event, Sci. Total Environ., 734, 139415, https://doi.org/10.1016/j.scitotenv.2020.139415, 2020b.

Lu, S., Win, M. S., Zeng, J., Yao, C., Zhao, M., Xiu, G., Lin, Y., Xie, T., Dai, Y., Rao, L., Zhang, L., Yonemochi, S., and Wang, Q.: A characterization of HULIS-C and the oxidative potential of HULIS and HULIS-Fe(II) mixture in $PM_{2.5}$ during hazy and non-hazy days in Shanghai, Atmos. Environ., 219, 117058, https://doi.org/10.1016/j.atmosenv.2019.117058, 2019.

Lu, T.: A comprehensive electron wavefunction analysis toolbox for chemists, Multiwfn, J. Chem. Phys., 161, 082503, https://doi.org/10.1063/5.0216272, 2024.

Lu, T. and Chen, F.: Multiwfn: A multifunctional wavefunction analyzer, J. Comput. Chem., 33, 580−592, https://doi.org/10.1002/jcc.22885, 2011.

Ma, L., Li, Z., Yabo, S. D., Li, B., Sun, S., and Qi, H.: Insight into the interaction between heavy metals and water-soluble organic compounds in $PM_{2.5}$ affected by heavy haze using ultraviolet−visible and fluorescence spectra combined with two-dimensional correlation spectroscopy, J. Clean. Prod., 362, 132476, https://doi.org/10.1016/j.jclepro.2022, 2022.

Ma, W., He, J., Han, L., Ma, C., Cai, Y., Guo, X., and Yang, Z.: Hydrophilic fraction of dissolved organic matter largely facilitated microplastics photoaging: Insights from redox properties and reactive oxygen species, Environ. Sci. Technol., 58, 11625−11636, https://doi.org/10.1021/acs.est.3c11111, 2024.

Moreno, T., Querol, X., Alastuey, A., Reche, C., Cusack, M., Amato, F., Pandolfi, M., Pey, J., Richard, A., Prévôt, A. S. H., Furger, M., and Gibbons, W.: Variations in time and space of trace metal aerosol concentrations in urban areas and their surroundings, Atmos. Chem. Phys., 11, 9415−9430, https://doi.org/10.5194/acp-11-9415-2011, 2011.

Pan, Y., Ruan, X., Garg, S., Waite, T. D., Lei, Y., and Yang, X.: Copper inhibition of triplet-sensitized phototransformation of phenolic and amine contaminants, Environ. Sci. Technol., 54, 9980−9989, https://doi.org/10.1021/acs.est.0c01693, 2020.

Peng, J., Hu, M., Shang, D., Wu, Z., Du, Z., Tan, T., Wang, Y., Zhang, F., and Zhang, R.: Explosive secondary aerosol formation during severe haze in the North China Plain, Environ. Sci. Technol., 55, 2189−2207, https://doi.org/10.1021/acs.est.0c07204, 2021.

Qin, J., Zhang, L., Qin, Y., Shi, S., Li, J., Shu, Z., Gao, Y., Qi, T., Tan, J., and Wang, X.: Measurement report: Effects of transition metal ions on the optical properties of humic-like

substances (HULIS) reveal a structural preference–a case study of $PM_{2.5}$ in Beijing, China, Atmos. Chem. Phys., 24, 7575−7589, https://doi.org/10.5194/acp-24-7575-2024, 2024.

Ruzi, R., Zhang, M., Ablajan, K., and Zhu, C.: Photoredox-catalyzed deoxygenative intramolecular acylation of biarylcarboxylic acids: Access to fluorenones, J. Org. Chem., 82, 12834−12839, https://doi.org/10.1021/acs.joc.7b02197, 2017.

Salana, S., Yu, H., Dai, Z., Subramanian, P. S. G., Puthussery, J. V., Wang, Y., Singh, A., Pope, F. D., Leiva, G. M., Rastogi, N., Tripathi, S. N., Weber, R. J., and Verma, V.: Inter-continental variability in the relationship of oxidative potential and cytotoxicity with $PM_{2.5}$ mass, Nat. Commun., 15, 5263, https://doi.org/10.1038/s41467-024-49649-4, 2024.

Shiraiwa, M., Li, Y., Tsimpidi, A. P., Karydis, V. A., Berkemeier, T., Pandis, S. N., Lelieveld, J., Koop, T., and Pöschl, U.: Global distribution of particle phase state in atmospheric secondary organic aerosols, Nat. Commun., 8, 15002, https://doi.org/10.1038/ncomms15002, 2017.

Singh, D. K. and Gupta, T.: Role of ammonium ion and transition metals in the formation of secondary organic aerosol and metallo-organic complex within fog processed ambient deliquescent submicron particles collected in central part of Indo-Gangetic Plain, Chemosphere, 181, 725−737, https://doi.org/10.1016/j.chemosphere.2017.04.080, 2017.

Tang, R., Zhang, R., Ma, J., Song, K., Mabato, B. R. G., Cuevas, R. A. I., Zhou, L., Liang, Z., Vogel, A. L., Guo, S., and Chan, C. K.: Sulfate formation by photosensitization in mixed incense burning–sodium chloride particles: Effects of RH, light intensity, and aerosol aging, Environ. Sci. Technol., 57, 10295−10307, https://doi.org/10.1021/acs.est.3c02225, 2023.

Treacy, S. M. and Rovis, T.: Photoinduced ligand-to-metal charge transfer in base-metal catalysis, Synthesis, 56, 1967−1978, https://doi.org/10.1055/s-0042-1751518, 2024.

Tsona, N. T. and Du, L.: A potential source of atmospheric sulfate from O_2^--induced SO_2 oxidation by ozone, Atmos. Chem. Phys., 19, 649−661, https://doi.org/10.5194/acp-19-649-2019, 2019.

Wang, T., Liu, M., Liu, M., Song, Y., Xu, Z., Shang, F., Huang, X., Liao, W., Wang, W., Ge, M., Cao, J., Hu, J., Tang, G., Pan, Y., Hu, M., and Zhu, T.: Sulfate formation apportionment during winter haze events in North China, Environ. Sci. Technol., 56, 7771−7778, https://doi.org/10.1021/acs.est.2c02533, 2022.

Wang, W., Liu, Y., Wang, T., Ge, Q., Li, K., Liu, J., You, W., Wang, L., Xie, L., Fu, H., Chen, J., and Zhang, L.: Significantly accelerated photosensitized formation of atmospheric sulfate at the air-water interface of microdroplets, J. Am. Chem. Soc., 146, 6580−6590, https://doi.org/10.1021/jacs.3c11892, 2024.

Wang, W., Liu, M., Wang, T., Song, Y., Zhou, L., Cao, J., Hu, J., Tang, G., Chen, Z., Li, Z., Xu, Z., Peng, C., Lian, C., Chen, Y., Pan, Y., Zhang, Y., Sun, Y., Li, W., Zhu, T., Tian, H., and Ge, M.: Sulfate formation is dominated by manganese-catalyzed oxidation of SO_2 on aerosol surfaces during haze events, Nat. Commun., 12, 1993, https://doi.org/10.1038/s41467-021-22091-6, 2021a.

Wang, X., Qin, Y., Qin, J., Long, X., Qi, T., Chen, R., Xiao, K., and Tan, J.: Spectroscopic insight into the pH-dependent interactions between atmospheric heavy metals (Cu and Zn) and water-soluble organic compounds in $PM_{2.5}$, Sci. Total Environ., 767, 145261, https://doi.org/10.1016/j.scitotenv.2021.145261, 2021b.

Wang, X., Qin, Y., Qin, J., Yang, Y., Qi, T., Chen, R., Tan, J., and Xiao, K.: The interaction laws of atmospheric heavy metal ions and water-soluble organic compounds in $PM_{2.5}$ based on the excitation-emission matrix fluorescence spectroscopy, J. Hazard. Mater., 402, 123497, https://doi.org/10.1016/j.jhazmat.2020.123497, 2021c.

Wang, X., Gemayel, R., Hayeck, N., Perrier, S., Charbonnel, N., Xu, C., Chen, H., Zhu, C., Zhang, L., Wang, L., Nizkorodov, S. A., Wang, X., Wang, Z., Wang, T., Mellouki, A., Riva, M., Chen, J., and George, C.: Atmospheric photosensitization: A new pathway for sulfate formation, Environ. Sci. Technol., 54, 3114−3120, https://doi.org/10.1021/acs.est.9b06347, 2020.

Wang, Y., Zhang, Q., Jiang, J., Zhou, W., Wang, B., He, K., Duan, F., Zhang, Q., Philip, S., and Xie, Y.: Enhanced sulfate formation during China's severe winter haze episode in January 2013 missing from current models, J. Geophys. Res.-Atmos., 119, 10425−10440, https://doi.org/10.1002/2013JD021426, 2014.

Wu, X., Vu, T. V., Shi, Z., Harrison, R. M., Liu, D., and Cen, K.: Characterization and source apportionment of carbonaceous $PM_{2.5}$ particles in China-A review, Atmos. Environ., 189, 187−212, https://doi.org/10.1016/j.atmosenv.2018.06.025, 2018.

Xing, X., Li, Z., Wang, Y., Tian, Z., Liu, D., Cheng, J., and Hao, Z.: Synergistic catalytic

degradation of benzene and toluene on spinel MMn_2O_4 (MCo, Ni, Cu) catalysts, J. Environ. Sci., 154, 238−251, https://doi.org/10.1016/j.jes.2024.08.016, 2025.

Yan, M. and Korshin, G. V.: Comparative examination of effects of binding of different metals on chromophores of dissolved organic matter, Environ. Sci. Technol., 48, 3177−3185, https://doi.org/10.1021/es4045314, 2014.

Yang, H., Yang, W., Ma, J., and Han, C.: Heterogeneous photochemical uptake of SO_2 on typical brown carbon species: A significant sulfate source, Atmos. Environ., 324, 120425, https://doi.org/10.1016/j.atmosenv.2024.120425, 2024a.

Yang, S., Yang, H., Na, H., Zheng, J., Yang, W., and Han, C.: Quantitative relationships between physicochemical properties of organic carbon from coal combustion and heterogeneous photooxidation of SO_2 to sulfates, J. Hazard. Mater., 495, 139132, https://doi.org/10.1016/j.jhazmat.2025.139132, 2025.

Yang, W., Zhang, T., Han, C., Tang, N., Yang, H., and Xue, X.: Photoenhanced heterogeneous reaction of O_3 with humic acid: Focus on O_3 uptake and changes in the composition and optical property, Environ. Pollut., 268, 115696, https://doi.org/10.1016/j.envpol.2020.115696, 2021.

Yang, W., Xia, Z., Zheng, J., Li, F., Nan, X., Du, T., and Han, C.: Reactive oxygen species play key roles in the nitrite formation by the inorganic nitrate photolysis in the presence of urban water-soluble organic carbon, Sci. Total Environ., 946, 174203, https://doi.org/10.1016/j.scitotenv.2024.174203, 2024b.

Zhang, F., Wang, Y., Peng, J., Chen, L., Sun, Y., Duan, L., Ge, X., Li, Y., Zhao, J., Liu, C., Zhang, X., Zhang, G., Pan, Y., Wang, Y., Zhang, A. L., Ji, Y., Wang, G., Hu, M., Molina, M. J., and Zhang, R.: An unexpected catalyst dominates formation and radiative forcing of regional haze, P. Natl. Acad. Sci. USA, 117, 3960−3966, https://doi.org/10.1073/pnas.1919343117, 2020a.

Zhang, P., Chen, T., Ma, Q., Chu, B., Wang, Y., Mu, Y., Yu, Y., and He, H.: Diesel soot photooxidation enhances the heterogeneous formation of H_2SO_4, Nat. Commun., 13, 5364, https://doi.org/10.1038/s41467-022-33120-3, 2022.

Zhang, P., Wang, Y., Chen, T., Yu, Y., Ma, Q., Liu, C., Li, H., Chu, B., and He, H.: Insight into the mechanism and kinetics of the heterogeneous reaction between SO_2 and NO_2 on diesel

744 black carbon under light irradiation, Environ. Sci. Technol., 57, 17718−17726,
745 https://doi.org/10.1021/acs.est.2c09674, 2023.
746 Zhang, P., Chen, H. C., Zhu, H., Chen, K., Li, T., Zhao, Y., Li, J., Hu, R., Huang, S., Zhu, W.,
747 Liu, Y., and Pan, Y.: Inter-site structural heterogeneity induction of single atom Fe catalysts
748 for robust oxygen reduction, Nat. Commun., 15, 2062, https://doi.org/10.1038/s41467-024-
749 46389-3, 2024.
750 Zhang, Q., Shen, Z., Zhang, L., Zeng, Y., Ning, Z., Zhang, T., Lei, Y., Wang, Q., Li, G., Sun,
751 J., Westerdahl, D., Xu, H., and Cao, J.: Investigation of primary and secondary particulate
752 brown carbon in two chinese cities of Xi'an and Hong Kong in wintertime, Environ. Sci.
753 Technol., 54, 3803−3813, https://doi.org/10.1021/acs.est.9b05332, 2020b.
754 Zhang, R. and Chan, C. K.: Simultaneous formation of sulfate and nitrate via co-uptake of SO_2
755 and NO_2 by aqueous NaCl droplets: Combined effect of nitrate photolysis and chlorine
756 chemistry, Atmos. Chem. Phys., 23, 6113−6126, https://doi.org/10.5194/acp-23-6113-2023,
757 2023.
758 Zhang, Y., Bao, F., Li, M., Chen, C., and Zhao, J.: Nitrate-enhanced oxidation of SO_2 on mineral
759 dust: A vital role of a proton, Environ. Sci. Technol., 53, 10139−10145,
760 https://doi.org/10.1021/acs.est.9b01921, 2019.
761 Zhang, Y., Bao, F., Li, M., Xia, H., Huang, D., Chen, C., and Zhao, J.: Photoinduced uptake
762 and oxidation of SO_2 on Beijing urban $PM_{2.5}$, Environ. Sci. Technol., 54, 14868−14876,
763 https://doi.org/10.1021/acs.est.0c01532, 2020c.
764 Zhang, Y., Wen, L., Chen, J., Wang, X., Xue, L., Yang, L., Wang, L., Li, Z., Yu, C., Chen, T.,
765 and Wang, W.: Trend in fine sulfate concentrations and the associated secondary formation
766 processes at an urban site in North China, Aerosol Air Qual. Res., 18, 1519−1530,
767 https://doi.org/10.4209/aaqr.2017.10.0358, 2018.
768 Zheng, B., Zhang, Q., Zhang, Y., He, K. B., Wang, K., Zheng, G. J., Duan, F. K., Ma, Y. L., and
769 Kimoto, T.: Heterogeneous chemistry: A mechanism missing in current models to explain
770 secondary inorganic aerosol formation during the January 2013 haze episode in North China,
771 Atmos. Chem. Phys., 15, 2031−2049, https://doi.org/10.5194/acp-15-2031-2015, 2015.
772 Zhu, J., Sheng, M., Shang, J., Kuang, Y., Shi, X., and Qiu, X.: Photocatalytic role of
773 atmospheric soot particles under visible-light irradiation: Reactive oxygen species

774 generation, self-oxidation process, and induced higher oxidative potential and cytotoxicity,
775 Environ. Sci. Technol., 56, 7668−7678, https://doi.org/10.1021/acs.est.2c00420, 2022.